

## MOLECULAR OUTFLOWS IN W5

ADAM GINSBURG AND JOHN BALLY

Center for Astrophysics and Space Astronomy, Department of Astrophysical and Planetary Sciences  
 University of Colorado and  
 389 UCB, Boulder, CO 80309-0389

JONATHAN P. WILLIAMS

Institute for Astronomy  
 University of Hawaii and  
 2680 Woodlawn Dr. Honolulu, HI 96822  
*Draft version January 9, 2010*

### ABSTRACT

New Bolocam 1.1mm and HARP CO 3-2 observations of the W5 star forming complex are presented. The first deep survey of molecular outflows in W5 has been extracted from the CO data. The majority of millimeter sources above a mass of  $M = 100M_{\odot}$  are associated with outflows or 24 micron point sources, indicating that nearly all of the dense ( $n \gtrsim 10^3 \text{ cm}^{-3}$ ) gas in W5 is forming stars.

*Subject headings:* jets and outflows — ISM: kinematics and dynamics — ISM: individual: W5 — stars: formation

### 1. INTRODUCTION

Galactic-scale shocks such as spiral density waves promote the formation of giant molecular clouds (GMCs) where massive stars, star clusters, and OB associations form. The massive stars in such groups can either disrupt the surrounding medium or promote further star formation. While ionizing and soft UV radiation, stellar winds, and eventual supernova explosions tend to destroy clouds in the immediate vicinity of massive stars, as the resulting bubbles age and decelerate, they can trigger further star formation. In the “collect and collapse” scenario (e.g. Elmegreen & Lada 1977), gas swept-up by expanding bubbles can collapse into new star-forming clouds. In the “radiation-driven implosion” (Bertoldi & McKee 1990; Klein et al. 1983), pre-existing clouds may be compressed by photo-ablation or by the increased pressure as they are overrun by an expanding shell. In some circumstances, forming stars are simply exposed as low-density gas is removed by the action of massive stars. These processes may play significant roles in determining the efficiency of star formation in clustered environments Elmegreen (1998).

Feedback from low mass stars may also control the shape of the stellar initial mass function in clusters (Adams & Fatuzzo 1996). Low mass young stars generate high velocity, collimated outflows that may also contribute to the turbulent support of a gas clump, preventing the clump from forming stars before it is blown away by O-stars. It is therefore important to understand whether the high or low mass stars form first.

The W5 star forming complex in the outer galaxy is a prime location to study massive star formation and triggering. The bright-rimmed clouds in W5 have been recognized as good candidates for ongoing triggering by a number of groups (Lefloch et al. 1997; Thompson et al. 2004; Karr & Martin 2003). The clustering properties

were analyzed by Koenig et al. (2008) using Spitzer infrared data, and a number of significant clusters were discovered. The whole W5 complex may be a product of triggering, as it is located on one side of the W4 chimney thought to be created by a supernova explosion  $\sim 10$  MYr ago (Oey et al. 2005).

The W5 complex was mapped in the CO 1-0 emission line by the FCRAO using the SEQUOIA receiver array (Heyer & Terebey 1998). Some early work was done to search for outflows in W5 (Bretherton et al. 2002), but the low-resolution CO 1-0 data only showed a few outflows. Higher excitation lines are better suited to the discovery of outflows because outflows tend to have low filling factors but high excitation temperatures, and they stand out better against the lower background at higher energy transitions.

Outflows are a ubiquitous indicator of the presence of ongoing star formation (Reipurth & Bally 2001). CO outflows are an indicator of ongoing embedded star formation at a younger stage than optical outflows because shielding from the interstellar radiation field is required for CO to survive. Although Herbig-Haro shocks and H<sub>2</sub> knots reveal the locations of the highest-velocity segments of these outflows, CO serves as a “calorimeter” measuring the majority of the mass and momentum ejected from protostars.

### 2. OBSERVATIONS

#### 2.1. Heterodyne

CO 3-2 345 GHz data was acquired at the JCMT using the HARP array on a series of observing runs. On January 2-4, 2008,  $\sim 800$  square arcminutes were mapped and  $\tau_{225}$  ranged from 0.1 to 0.4. Additional areas were mapped on August 4-7, October 16-20 and 31, and Nov 1, 12-15 in similar conditions. A total of  $\sim 2$  square degrees in the W5 complex were mapped.

In January 2008, 14 of the 16 detectors were functional. In the 2nd half of 2008, 12 of 16 were functional, necessitating slightly longer scans to achieve similar S/N.

A raster mapping strategy was used. The array was shifted by 1/2 of a pixel spacing (7'') between scans to achieve full sampling. Two perpendicular scans were used for each patch observed. Most patches were 10×10' and took ~ 45 minutes.

Data was reduced using the STARLINK package. MAKECUBE was used to generate mosaics of contiguous sub-fields. A linear fit was subtracted from each spectrum over emission-free velocities to remove the baseline.

### 2.2. BGPS

The Bolocam Galactic Plane Survey (Aguirre et al. 2009; Rosolowsky et al. 2009) is a 1.1 mm continuum survey of the first quadrant and selected regions in the second and third quadrant. It reached a variable depth in the W5 region from RMS ~ 30-60 mJy/beam. The BGPS is sensitive to spatial scales in the range 30-150'', or 0.3-1.5 pc at a distance of 2 kpc.

### 2.3. FCRAO OGS

The Five College Radio Astronomy Observatory (FCRAO) Outer Galaxy Survey (OGS) observed the W5 complex in  $^{12}\text{CO}$  and  $^{13}\text{CO}$  1-0 (Heyer et al. 1998). The  $^{13}\text{CO}$  data cube achieved a mean sensitivity of 0.35 K per 0.13 km s $^{-1}$  channel, or 0.6 K km s $^{-1}$  integrated. The  $^{13}\text{CO}$  cube was integrated over all velocities and re-sampled to match the BGPS map using the MONTAGE<sup>1</sup> package.

### 2.4. Spitzer

Spitzer IRAC and MIPS 24  $\mu\text{m}$  images from Koenig et al. (2008) were used for morphological comparison. Their catalog was used to match outflows to potential sources.

## 3. ANALYSIS

### 3.1. CO 3-2

The measured outflow properties and source associations are presented in Table ???. The velocity centers were computed by fitting a gaussian to the  $^{13}\text{CO}$  spectrum at the outflow location. The widths were measured by eye from position-velocity diagrams and extracted spectra and are therefore full-width zero-power measurements. The column density for CO J=3-2 is estimated using the equation

$$N_{\text{H}_2} = \frac{\text{H}_2}{\text{CO}} \frac{8\pi\nu^3 k_B}{3c^3 h B_e A_{ul}} (1 - e^{h\nu/k_B T_{ex}})^{-1} \frac{1}{\eta_{mb}} \int T_A^*(v) dv \quad (1)$$

where  $A_{ul} = A_{32} = 2.5 \times 10^{-6} \text{s}^{-1}$  (Turner et al. 1977), the rotational constant  $B_e = 57.64 \text{ GHz}$  for  $^{12}\text{CO}$ ,  $\eta_{mb} = .68$ , and  $T_{ex}$  is assumed to be 20K. The partition function is approximated as

$$Z = \sum_{J=1}^{\infty} (2J+1) \exp\left(\frac{-J(J+1)hB_e}{k_B T_{ex}}\right) \approx \int_0^{\infty} (2J+1) \exp\left(\frac{-J(J+1)hB_e}{k_B T_{ex}}\right) dJ \quad (2)$$

which is valid when  $T_{ex} \gg hB_e/k_B \sim 2.8\text{K}$ . Equation 1 becomes

$$N_{\text{H}_2} = (3.27 \times 10^{18} \text{cm}^{-2}) \frac{1}{\eta_{mb}} \int T_A^*(v) dv \quad (3)$$

<sup>1</sup> <http://montage.ipac.caltech.edu/>

where the integrand is in units K km s $^{-1}$ . The mass is then

$$M = \mu m_{\text{H}_2} A N_{\text{H}_2} = 1.42 \times 10^{-5} A \frac{1}{\eta_{mb}} \int T_A^*(v) dv \quad (4)$$

where  $A$  is the area in cm $^2$ ,  $\mu = 1.4$  is a constant to account for the presence of helium, and again velocity is in km s $^{-1}$ .

All of the contour maps presented (in the online edition?) have contours at .5, 1, 1.5, 2, 3, 4, 5, 6, 8, 10, 12, 14, 16, 18, 20, 25, 30, 35, 40, 45, 50, 60, 70, 80, 90, 100 K km s $^{-1}$ . The integration ranges are indicated in the titles. The red and blue X's indicate the center of the ellipse used to extract the spectra. They are frequently offset from the center of the contours because the ellipses were selected to incorporate emission at all velocities in the outflows, but many have spatial gradients.

### 3.2. $^{13}\text{CO}$ 1-0

The  $^{13}\text{CO}$  column was computed using

$$N = 1.694e20 / (1 - e^{(-5.3/T_{ex})}) \int T_{mb} dv \text{cm}^{-2} \quad (5)$$

, where we have assumed the excitation temperature  $T_{ex} = T_K = 20 \text{ K}$ . The  $1 - \sigma$  column sensitivity limit is  $4.4 \times 10^{20} \text{ cm}^{-2}$  or  $0.16 M_{\odot}$  for an assumed 2 kpc distance in 22.5'' square pixels.

In addition, the MONTAGE package was used to match the  $^{13}\text{CO}$  map to the 1.1 mm map and both were converted into column density maps to compare morphologies on the same flux scale (see section 4.1).

### 3.3. 1.1 mm continuum

The 1.1 mm continuum is converted to a column density using

$$N = 2.19 \times 10^{22} * (\exp(13.01/T_{ex}) - 1) \frac{F_{\nu}}{1 \text{ Jy}} \text{cm}^{-2} \quad (6)$$

(Aguirre et al. 2009). The  $1 - \sigma$  column sensitivity (using the average RMS of 38 mJy/beam) is  $7.6 \times 10^{20} \text{ cm}^{-2}$  or  $2.0 M_{\odot}$  in 7.2'' square pixels.

## 4. RESULTS

We have identified 38 outflows from the CO 3-2 data. Their positions and polarities (red or blue shifted relative to the ambient cloud) are displayed in Figure 2. We used  $^{13}\text{CO}$  to determine the central velocities of the outflows and measure momentum and energy from those central velocities.

### 4.1. Dense vs. diffuse mass

The total mass computed from  $^{13}\text{CO}$  is  $2.6 \times 10^4 M_{\odot}$  from summing over all pixels  $> 1\sigma \sim 0.6 \text{ K km s}^{-1}$  and accounting for statistical bias. The 1.1 mm mass is  $3.1 \times 10^3 M_{\odot}$  at  $1\sigma \sim 38 \text{ mJy}$  ( $\sim 1 M_{\odot}$ ). The  $^{13}\text{CO}$  mass estimate is approximately consistent with the  $6.5 \times 10^4 M_{\odot}$  derived by Koenig et al. (2008) from a 2MASS extinction map; it may be lower because the  $^{13}\text{CO}$  has a high column-density sensitivity cutoff when it becomes optically thick. The 1.1 mm /  $^{13}\text{CO}$  mass ratio is  $\sim 10\%$ , but this discrepancy is entirely due to filtering.

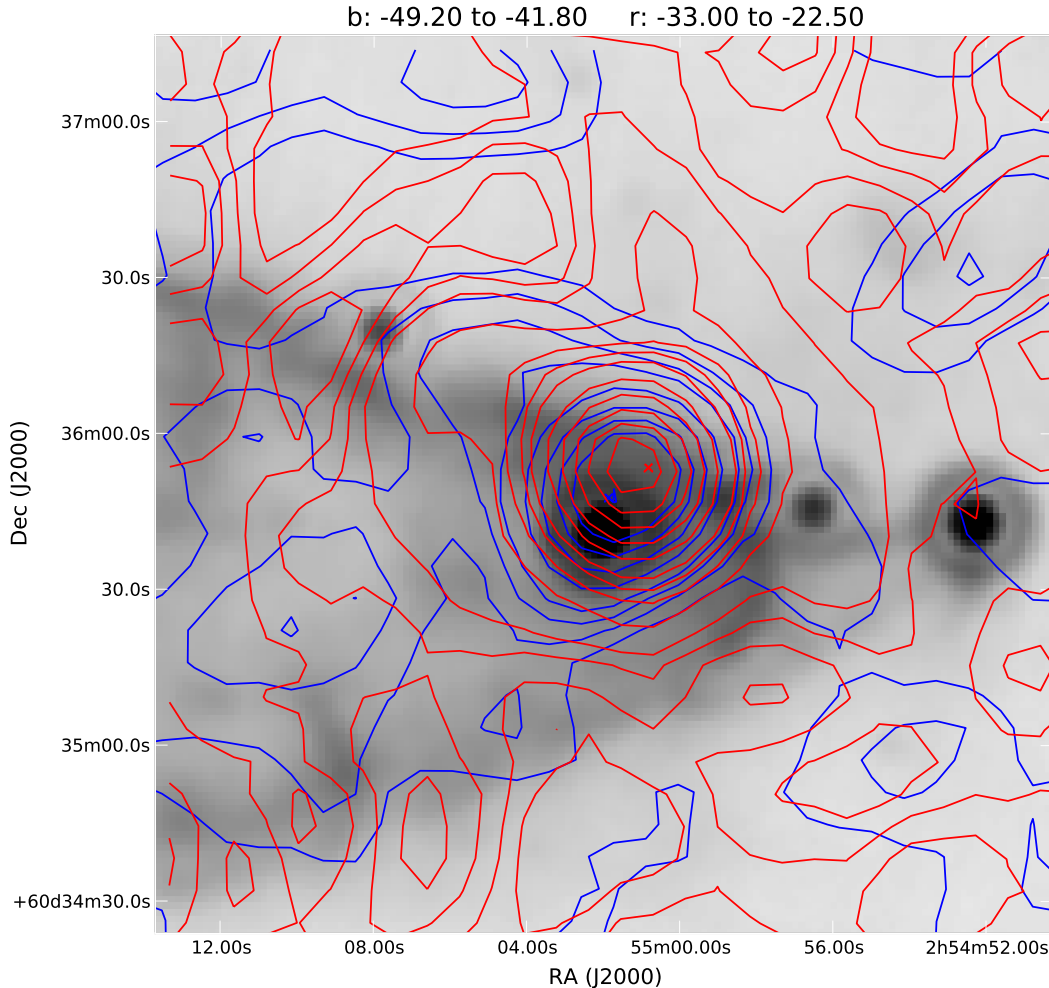


FIG. 1.— CO 3-2 integrated over velocities integrated in Table ?? overlaid on the MIPS 24  $\mu\text{m}$  image. This example shows outflows 25 and 26 associated with BGPS source G137.538+01.278.

## 5. OUTFLOWS

We have detected 38 distinct outflows in the CO 3-2 data cubes. Outflows are identified by the presence of high-velocity, spatially compact wings. Automated detection is not possible because confusing signatures - e.g. multiple clouds at slightly different velocities - would appear the same as outflows to an automated search. Emission lines that could be well-fit by Gaussians without tails, i.e. separate low-velocity cloud components, were not selected as outflows.

Of these outflows, all except 2 are at least loosely associated with a peak in the Bolocam 1.1mm emission. One of these two (outflow 38) is outside of the BGPS mapped area. The other, Outflow 33, is centered on a bright 24  $\mu\text{m}$  source (17125) that lines up with a weak hole in the  $^{13}\text{CO}$  integrated intensity map.

The flow properties have low averages with high outliers. Typical values are  $E = 1 \times 10^{43}$  ergs,  $M = 0.02 M_{\odot}$ ,  $p = 0.12 M_{\odot} \text{km s}^{-1}$ , and  $N = 4 \times 10^{18} \text{cm}^{-2}$ . These val-

ues are likely to be close to the outflow detection limit in our survey, as the distribution appears to increase towards lower values of energy/ momentum/mass/column with a turnover around the lowest detected. The total measured outflow mass is  $1.0 M_{\odot}$ , while the total outflow momentum is  $8.1 M_{\odot} \text{km s}^{-1}$ . Assuming a turbulent line width  $\Delta v \sim 3 \text{km/s}$ , the total turbulent momentum  $p = 7.8 e 4 M_{\odot} \text{km s}^{-1}$ , which is very nearly  $10^4$  times the current outflow momentum.

## 6. NOTES ON INDIVIDUAL OUTFLOWS - DISCUSSION OF ASSOCIATIONS

Spitzer measurements from Koenig et al. (2008) are used to classify sources as Class I/II protostars. For sources clearly associated with CO outflows, we have used the model fitting code from Robitaille et al. (2007) to attempt to determine the stellar mass. The SED fitter was used with inputs from 2MASS, IRAC, and MIPS data for all sources, and MSX data for the most luminous 24  $\mu\text{m}$  sources that were saturated in MIPS images.

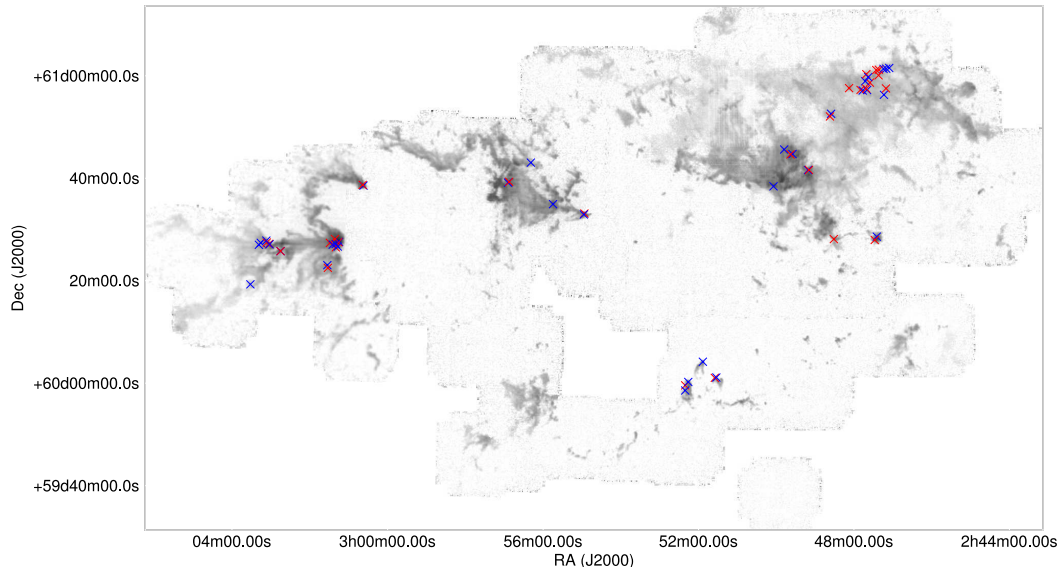


FIG. 2.— A mosaic of the CO 3-2 data cube integrated from -20 to -60 km s<sup>-1</sup>. The grayscale is linear from 0 to 150 K km s<sup>-1</sup>. The red and blue X's mark the locations of redshifted and blueshifted outflows.

In addition, IRAS point source catalog fluxes and measured IRAS surface brightnesses were used as upper limits. SCUBA 850  $\mu$ m point sources were included when they matched, and Bolocam 1.1mm fluxes were used as upper limits because of poor resolution matching to the Spitzer stars.

Any outflows with mid-IR source associations or caveats are discussed in this section.

1 - Elongated on the plane of the sky. This outflow appears to be a classic bipolar outflow. Center is in a region of  $\sim 2\sigma$  BGPS emission.

3 - 2MASS 02470551+6102451 is also IRAS 02431+6050

8 - Has odd shape in p-v space: could be a series of clouds at different velocities. It is not associated with a BGPS source because the BGPS emission here is patchy and therefore too inconsistent to form a single 'source' for extraction; however there clearly is dust emission at this point. The red outflow is very high significance, while the blue is low; the velocity center is shifted to the red so the blue may simply be lost in the local cloud.

10 - 1100? - Class I. Isolated, IRAS luminosity  $\sim 800 L_{\odot}$  (Karr & Martin 2003).

13 - 2MASS 02492991+6047287 is an uncataloged 24  $\mu$ m source. The blue outflow is lost in an adjacent cloud.

16 - The blue contours near the red outflow are a separate blob at the same velocity as the blue outflow. The blob's shape is not consistent with other outflows (i.e. it is Gaussian, not a line wing). 30 appears to be associated with 5697 (Class I), but 29 has no association and there is no source at the midpoint.

18 - 32 may be associated with 6733 (Class I), but there is no source at the 32-33 midpoint.

25 - 16614 - Class II. IRAS luminosity  $\sim 540 L_{\odot}$  (Karr & Martin 2003). Confused / clustered.

26 - The region centered on AFGL 4029 is highly confused. At least 3 distinct outflows are detected, but it was not possible to determine the red/blue pairings uniquely except in the case of 26. Outflow 26 is associated with 17020 (Class I). The IRAS luminosity is  $\sim 6.5 \times 10^3 L_{\odot}$  (Karr & Martin 2003), although de Wit et al. (2009) acquire a best fit luminosity of  $1.1\text{-}1.2 \times 10^4 L_{\odot}$ .

27 - The contours are blended with outflow 26 but this is a unique outflow in position-velocity space.

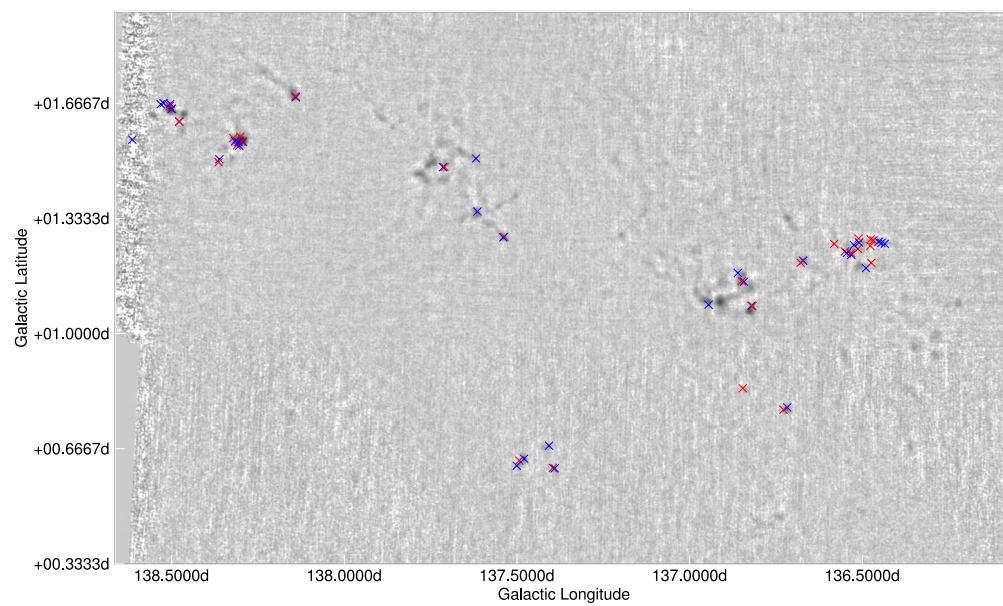
33 - This is the only CO outflow pair that does not correspond to BGPS emission. It has a clear 24  $\mu$ m source, 17125 (Class I). Based on the <sup>13</sup>CO, this object may be missed because it is surrounded by diffuse emission at a very similar level and therefore gets filtered out by the Bolocam spatial filter.

34 - While there is some high-velocity emission, the shape of this object in position-velocity space is not quite like other outflows. This object may simply be a CO 3-2 blob moving at a slightly different velocity than the cloud.

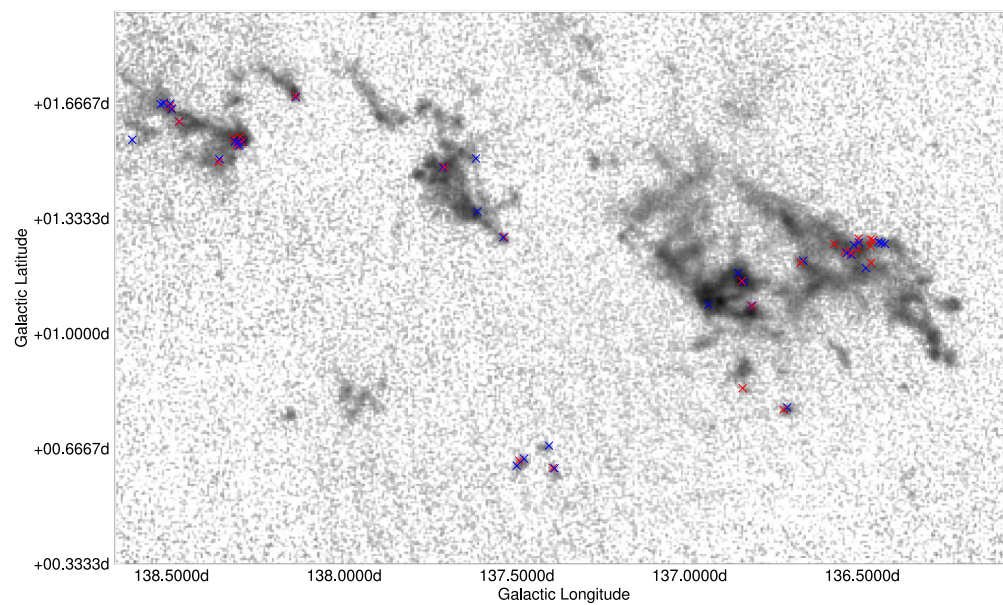
37 - There is no clear source for this outflow, and it appears to be outside the Sh 2-201 HII region. The <sup>13</sup>CO cloud extends out to include this outflow while the dust clump does not; this may indicate the dust in this part of the cloud is thin enough that ice mantles have been destroyed or were unable to form, reducing the dust emissivity. Alternately, it is possible that there is an isolated protostellar core with no associated envelope.

38 - This outflow is not associated with W5, but is at a kinematic distance of 5.5 kpc.

## 7. DISCUSSION

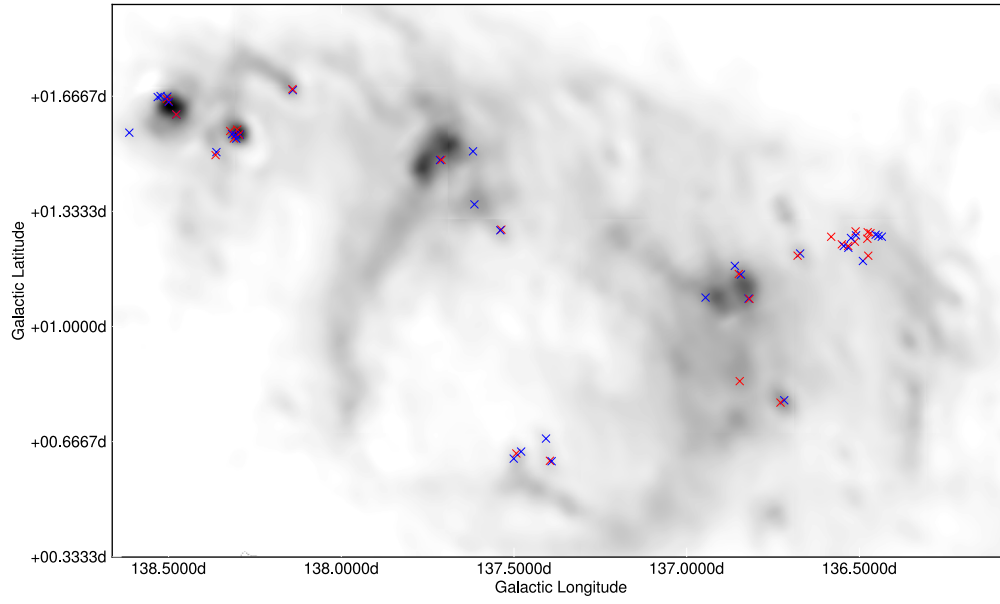


(a)

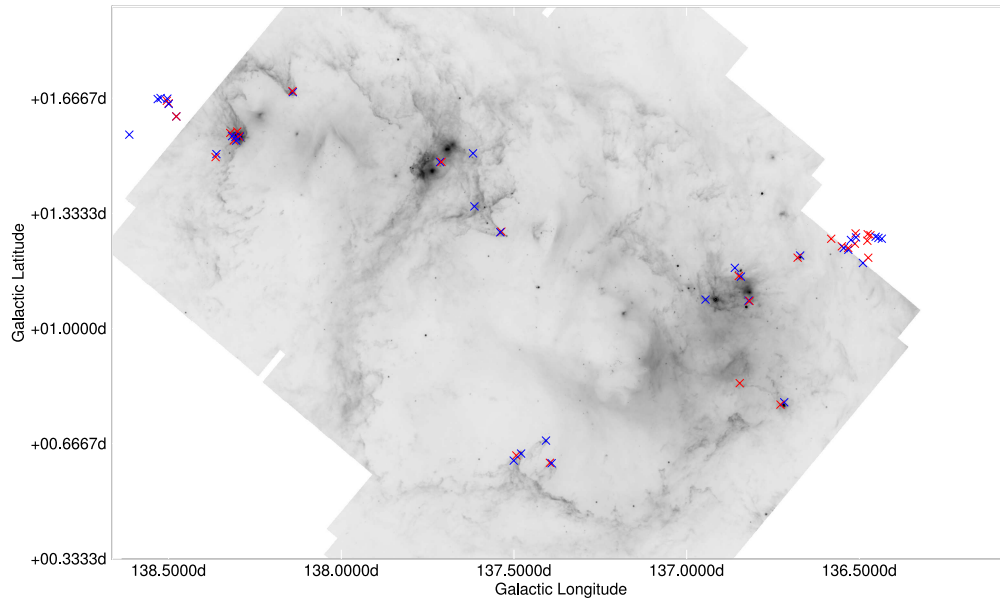


(b)





(c)



(d)

FIG. 2.— Grayscale images are shown with a logarithmic stretch to enhance faint features. (a) BGPS 1.1mm emission from  $-0.05$  to  $1.0$  Jy/beam. (b)  $^{13}\text{CO}$  integrated intensity from  $0$  to  $15$  K km s $^{-1}$ . (c) IRAS  $100\text{ }\mu\text{m}$  from  $25$  to  $800$  MJy sr $^{-1}$ . (d) Spitzer  $24\text{ }\mu\text{m}$  from  $800$  to  $8000$  MJy sr $^{-1}$ . The red and blue ellipses indicate the presence of red and blueshifted CO 3-2 outflows.

We have divided the W5 region into distinct sub-regions plus unclustered objects that all show signs of star formation. The AFGL 4029, LW Cas Nebula, IC 1848, and the southern pillar sub-regions are all along the edge of the diffuse HII regions that shape W5. In these sub-regions, the radiation pressure from the O-stars could have led to triggered collapse. However, there are also outflows in Sh 201 and W5 NW, which are not adjacent to the HII region and do not show signs of external pressure.

### 7.1. Star Formation Activity

Outflows are an excellent tracer of ongoing embedded star formation. We use the locations of newly discovered outflows to qualitatively determine the star formation activity within the W5 complex and evaluate the hypothesis that star formation has been triggered on small or intermediate scales.

#### 7.1.1. Sh 2-201

Sh 2-201 is part of the same molecular cloud as the BRCs in W5E, but it does not share a cometary shape with these clouds. Instead, it is internally heated and has its own HII region. It must therefore have begun the star forming process before radiation driven shocks from the W5 O-stars could have impacted it. There are 4 bipolar CO outflows associated with this region, 3 of which are on or near G138.502+01.646. The other is near, but not directly associated with, G138.463+01.632. The outflows come primarily from the 8  $\mu$ m- faint part of the region, likely because the 8  $\mu$ m emission traces a blown out gas-poor cavity.

#### 7.1.2. AFGL 4029

AFGL 4029 is a young cluster embedded in a cometary cloud. It is the brightest and most massive millimeter source in W5. There is one clear bipolar outflow and 6 single-direction flows than cannot be unambiguously associated with an opposite direction counterpart. The cluster is mostly unresolved in the data sets presented here.

#### 7.1.3. W5 Ridge

The “Ridge” separating the east and west lobes of W5 contains the LW Cas nebula on its east side and an X-shaped nebula on the west. The east portion of LW Cas Nebula is bright in both the continuum and CO 3-2 but lacks outflows (see Figure 5). It is likely to be pressure-confined, externally heated hot dust: while the measured mass (assuming  $T=20K$ ) in each clump is  $\sim 1 - 200M_{\odot}$ , their inferred average densities are only  $\sim 10^3 cm^{-3}$ . The CO 3-2 FWHM line width in the clumps ranges from 3-4  $km s^{-1}$ , suggesting that the clumps are not bound (virial ratios range from 7-14).

The B1V star BD+60 596 is the probable source of the UV radiation heating this nebula, though the variable star V\* LW Cas, which is alternately identified as a cataclysmic variable (Seal 1995) and a FU Ori variable star (Wenzel & Fuhrmann 1983) could also be responsible for some of the local heating. The HII region emission is highly extinguished by the dust in the optical, and the CO emission is slightly blueshifted, so the UV radiation should be evaporating the back of the cloud. Without a

measurement of the mass-loss rate by photoevaporation, it is difficult to know if these clumps will have a chance to form stars before they are dispersed.

The X-shaped ridge contains less mass but shows evidence of distributed star formation. Both the center of the X and the cometary cloud on the southwest end of the X contain a CO outflow.

#### 7.1.4. Southern Pillars

There are 3 cometary clouds that resemble the “elephant trunk” nebula in IC 1396. Each of these pillars contains evidence of at least one outflow. These pillars are low-mass and isolated; there is no other dense gas in the southern part of W5.

#### 7.1.5. W5 Southwest

There are two isolated clumps associated with outflows in the southwest part of W5. They are at  $v_{LSR} \sim 45 km s^{-1}$  and are therefore likely to be associated with the rest of the W5W region.

#### 7.1.6. W5 West / IC 1848

IRAS 02459+6029 is the brightest IRAS point source in W5W. No outflow is observed in the CO 3-2 data. The nondetection may be due to confusion in this area - there are two layers of CO gas separated by  $\sim 5 km s^{-1}$ , so (low-velocity) outflow detection is more difficult. Alternately, there are long finger-like structures pointing away from the IRAS source that may suggest an outflow in the plane of the sky. The lack of an outflow likely indicates that this region has evolved past its CO-outflow stage.

The presense of two separate sheets confuses the physical association in this region. A velocity gradient is present in both sheets, but they are less separated in velocity on the side nearest the W5 O-stars, so it is unlikely that the sheets have been blown away from each other.

The BGPS source G136.828+01.064 ( $M_{1.1mm} \sim 220M_{\odot}$ ) is associated with a deeply embedded cluster and 5 Class I objects from Koenig et al. (2008). This location marks the worst velocity confusion in CO but contains hints that there may be outflows. The source is a good candidate for high-resolution follow-up.

#### 7.1.7. W5 NW

The northwest cluster containing outflows 1-8 is at a different velocity than the majority of the W5 cloud complex. It may therefore be separated along the line of sight. The presence of significant star formation activity as evidenced by the outflow cluster suggests that the region, even if distinct from W5, is co-eval to within  $\sim 5$  Myr. If the cluster is associated with the W5 region, its presence suggests that small- to intermediate-scale triggering is not responsible for the current generation of star formation throughout W5: this cluster shows much lower CO surface temperatures and weaker Spitzer 8 $\mu$ m emission than the “bright-rimmed clouds” (BRCs, Niwa et al. 2009; Sugitani et al. 1991) seen near the W5 O-stars and therefore has not been affected by their radiation. The presence of independent but co-eval star formation is, however, consistent with the large-scale “collect-and-collapse” scenario.

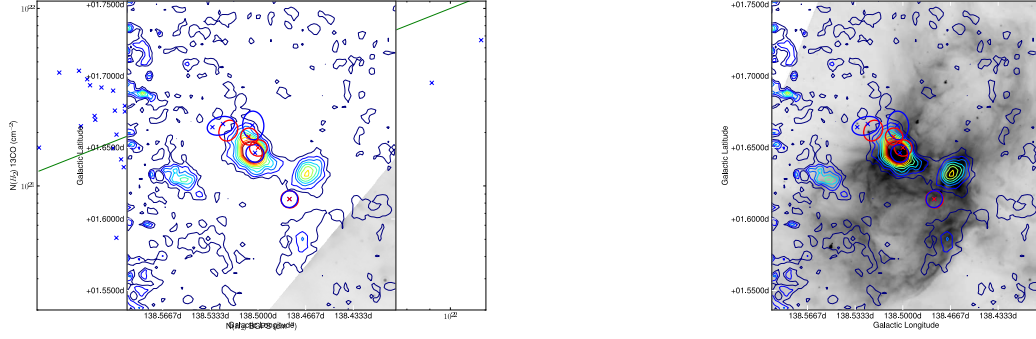


FIG. 3.— Zoom-in on the Sh 2-201 region. (left) The MIPS 24  $\mu\text{m}$  image is displayed inverted in log scale from 600 to 5000  $\text{MJy sr}^{-1}$ . (right) The IRAC 8  $\mu\text{m}$  image is displayed in inverted log scale from 800 to 8000  $\text{MJy sr}^{-1}$ . BGPS 1.1 mm contours are overlaid from 20 to 420  $\text{mJy beam}^{-1}$  in intervals of 40  $\text{mJy beam}^{-1}$ .



FIG. 4.— Zoom-in on the AFGL 4029 region. (left) The MIPS 24  $\mu\text{m}$  image is displayed inverted in log scale from 600 to 5000  $\text{MJy sr}^{-1}$ . (right) The IRAC 8  $\mu\text{m}$  image is displayed in inverted log scale from 800 to 8000  $\text{MJy sr}^{-1}$ . BGPS 1.1 mm contours are overlaid from 20 to 420  $\text{mJy beam}^{-1}$  in intervals of 40  $\text{mJy beam}^{-1}$ .

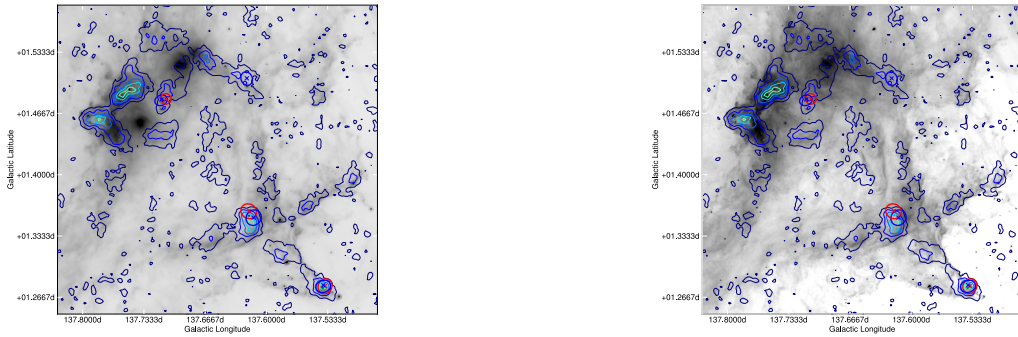


FIG. 5.— Zoom-in on the LW Cas nebula. (left) The MIPS 24  $\mu\text{m}$  image is displayed inverted in log scale from 600 to 5000  $\text{MJy sr}^{-1}$ . (right) The IRAC 8  $\mu\text{m}$  image is displayed in inverted log scale from 800 to 8000  $\text{MJy sr}^{-1}$ . BGPS 1.1 mm contours are overlaid from 20 to 420  $\text{mJy beam}^{-1}$  in intervals of 40  $\text{mJy beam}^{-1}$ . The 24  $\mu\text{m}$  source at  $J(2000) = 02:57:08.0233 +60:39:44.142$  is the B1V star BD+60 596.



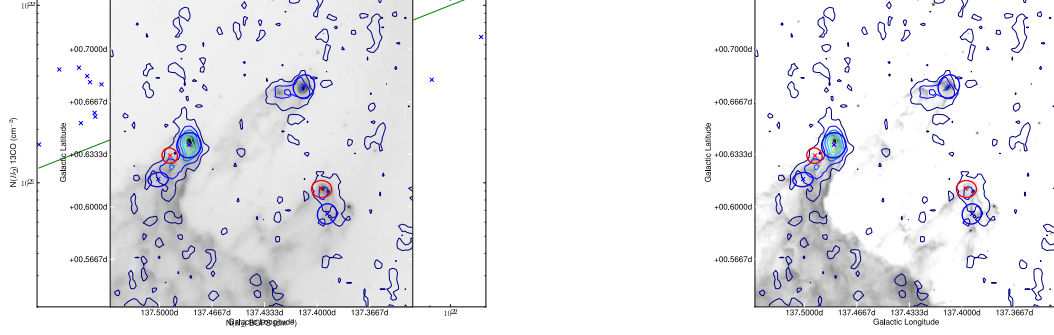


FIG. 6.— Zoom-in on the W5 S region. (left) The MIPS  $24\ \mu\text{m}$  image is displayed inverted in log scale from 600 to 5000  $\text{MJy sr}^{-1}$ . (right) The IRAC  $8\ \mu\text{m}$  image is displayed in inverted log scale from 800 to 8000  $\text{MJy sr}^{-1}$ . BGPS 1.1 mm contours are overlaid from 20 to 420  $\text{mJy beam}^{-1}$  in intervals of 40  $\text{mJy beam}^{-1}$ .

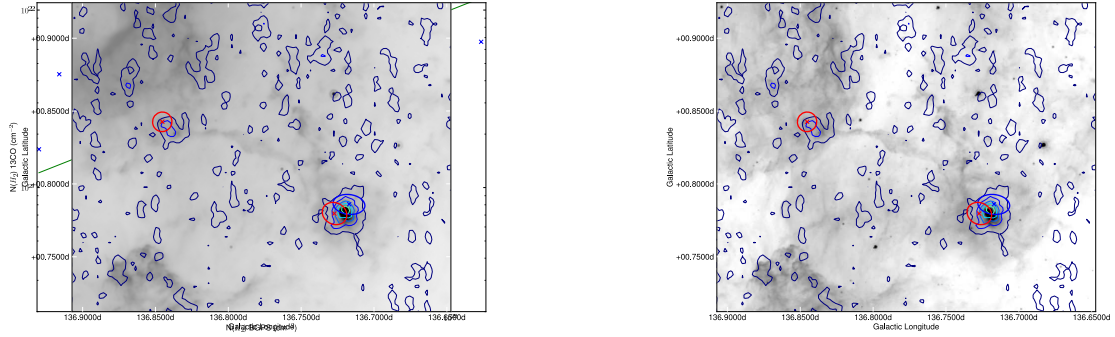


FIG. 7.— Zoom-in on the W5 SW region. (left) The MIPS  $24\ \mu\text{m}$  image is displayed inverted in log scale from 600 to 5000  $\text{MJy sr}^{-1}$ . (right) The IRAC  $8\ \mu\text{m}$  image is displayed in inverted log scale from 800 to 8000  $\text{MJy sr}^{-1}$ . BGPS 1.1 mm contours are overlaid from 20 to 420  $\text{mJy beam}^{-1}$  in intervals of 40  $\text{mJy beam}^{-1}$ .

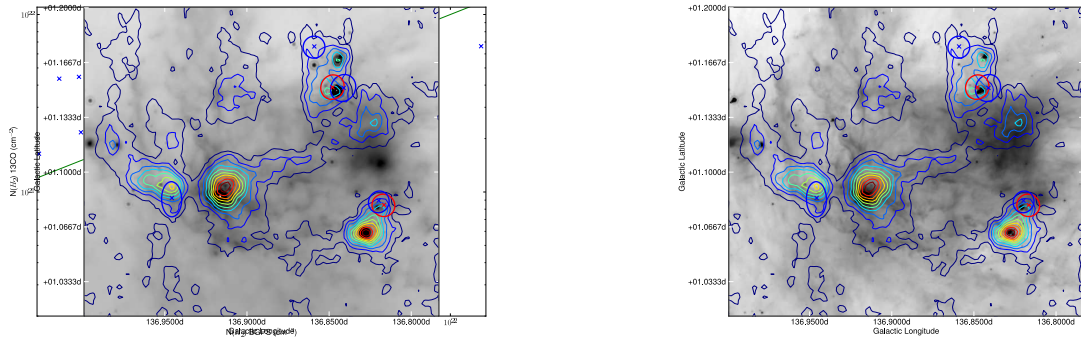


FIG. 8.— Zoom-in on the W5 W region. (left) The MIPS  $24\ \mu\text{m}$  image is displayed inverted in log scale from 600 to 5000  $\text{MJy sr}^{-1}$ . (right) The IRAC  $8\ \mu\text{m}$  image is displayed in inverted log scale from 800 to 8000  $\text{MJy sr}^{-1}$ . BGPS 1.1 mm contours are overlaid from 20 to 420  $\text{mJy beam}^{-1}$  in intervals of 40  $\text{mJy beam}^{-1}$ .

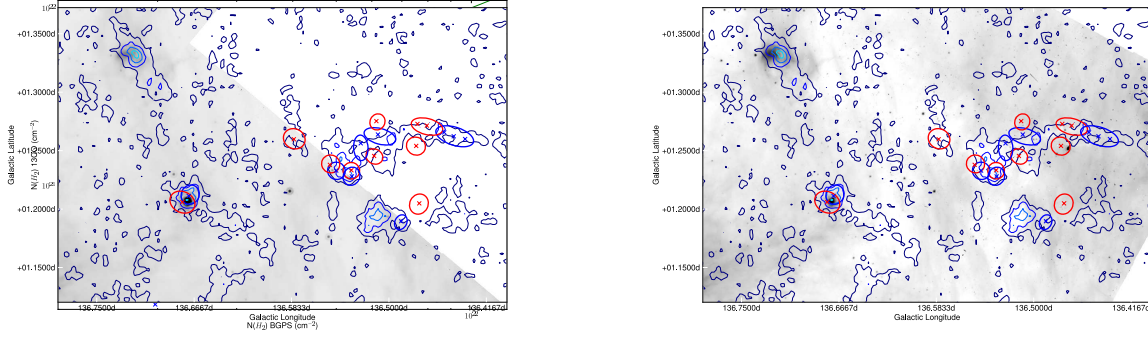


FIG. 9.— Zoom-in on the W5 NW region. (left) The MIPS 24  $\mu\text{m}$  image is displayed in log scale from 600 to 5000  $\text{MJy sr}^{-1}$ . (right) The IRAC 8  $\mu\text{m}$  image is displayed in inverted log scale from 800 to 8000  $\text{MJy sr}^{-1}$ . BGPS 1.1 mm contours are overlaid from 20 to 420  $\text{mJy beam}^{-1}$  in intervals of 40  $\text{mJy beam}^{-1}$ .

## 7.2. Outflow Properties

Outflows are observed with masses in the range  $2\text{--}60 \times 10^{-3} M_{\odot}$ . If a typical outflow lifetime is assumed to be  $\sim 10^4$  yr (Reipurth & Bally 2001), this translates into a mass-loss rate ranging from  $2 \times 10^{-7} M_{\odot} \text{yr}^{-1}$  to  $6 \times 10^{-7} M_{\odot} \text{yr}^{-1}$ . The momentum fluxes range from  $6 \times 10^{-7}$  to  $6 \times 10^{-5} M_{\odot} \text{km s}^{-1}$ , which nearly covers the complete range of momentum fluxes observed by Bontemps et al. (1996), though the luminosities hinted at by the IRAS maps are substantially higher. There may be a flattening of the momentum flux-luminosity correlation at higher luminosities.

## 8. CONCLUSIONS

We have identified 38 outflows and associated 25 of them with infrared counterparts in the W5 star forming complex.

- The majority of the millimeter sources are associated with outflows, though some of the brightest millimeter sources lack outflows. The lack of out-

flow activity is attributed to a later evolutionary state in these sources, which is consistent with their high far-infrared luminosities. Millimeter emission is a good tracer of active embedded star formation.

- CO 3-2 outflow activity shows that all regions containing multiple dense gas clumps in the W5 complex are actively forming stars. In addition, regions on the outskirts of the complex are also actively forming stars.
- Because star formation activity is observed outside of the region of influence of the W5 O-stars, it is apparent that the radiatively-driven implosion mechanism does not explain all of the star formation around W5.

## 9. ACKNOWLEDGEMENTS

This work has made use of the APLpy plotting package (<http://aplpy.sourceforge.net>) and the pyregion package (<http://leejjoon.github.com/pyregion/>). It was sup-

## REFERENCES

- Adams, F. C. & Fatuzzo, M. 1996, *ApJ*, 464, 256  
Aguirre, J., Ginsburg, A., & Team, B. 2009, In Prep  
Bertoldi, F. & McKee, C. F. 1990, *ApJ*, 354, 529  
Bontemps, S., Andre, P., Terebey, S., & Cabrit, S. 1996, *Astronomy and Astrophysics*, 311, 858  
Bretherton, D. E., Moore, T. J. T., & Ridge, N. A. 2002, in *Hot Star Workshop III: The Earliest Phases of Massive Star Birth*, Vol. 267, 347  
de Wit, W. J. et al. 2009, *Astronomy and Astrophysics*, 494, 157  
Elmegreen, B. G. 1998, in *Astronomical Society of the Pacific Conference Series*, Vol. 148, Origins, ed. C. E. Woodward, J. M. Shull, & H. A. Thronson Jr., 150+  
Elmegreen, B. G. & Lada, C. J. 1977, *ApJ*, 214, 725  
Heyer, M. H., Brunt, C., Snell, R. L., Howe, J. E., Schloerb, F. P., & Carpenter, J. M. 1998, *ApJS*, 115, 241  
Heyer, M. H. & Terebey, S. 1998, *ApJ*, 502, 265  
Karr, J. L. & Martin, P. G. 2003, *Astrophysical Journal*, 595, 900  
Klein, R. I., Sandford, II, M. T., & Whitaker, R. W. 1983, *ApJ*, 271, L69  
Koenig, X. P., Allen, L. E., Gutermuth, R. A., Hora, J. L., Brunt, C. M., & Muzerolle, J. 2008, *Astrophysical Journal*, 688, 1142  
Lefloch, B., Lazareff, B., & Castets, A. 1997, *Astronomy and Astrophysics*, 324, 249  
Niwa, T., Tachihara, K., Itoh, Y., Oasa, Y., Sunada, K., Sugitani, K., & Mukai, T. 2009, *Astronomy and Astrophysics*, 500, 1119  
Oey, M. S., Watson, A. M., Kern, K., & Walth, G. L. 2005, *Astronomical Journal*, 129, 393  
Reipurth, B. & Bally, J. 2001, *Annual Review of Astronomy and Astrophysics*, 39, 403  
Robitaille, T. P., Whitney, B. A., Indebetouw, R., & Wood, K. 2007, *Astrophysical Journal Supplement Series*, 169, 328  
Rosolowsky, E. et al. 2009, 0909.2871  
Seal, P. 1995, *Ap&SS*, 234, 223  
Sugitani, K., Fukui, Y., & Ogura, K. 1991, *Astrophysical Journal Supplement Series*, 77, 59  
Thompson, M. A., White, G. J., Morgan, L. K., Miao, J., Fridlund, C. V. M., & Hultgren-White, M. 2004, *Astronomy and Astrophysics*, 414, 1017  
Turner, J., Kirby-Docken, K., & Dalgarno, A. 1977, *ApJS*, 35, 281  
Wenzel, W. & Fuhrmann, B. 1983, *Zentralinstitut fuer Astrophysik Sternwarte Sonneberg Mitteilungen ueber Veraenderliche Sterne*, 9, 143

TO DO: -add associated source locations -make website showing sources? DONE

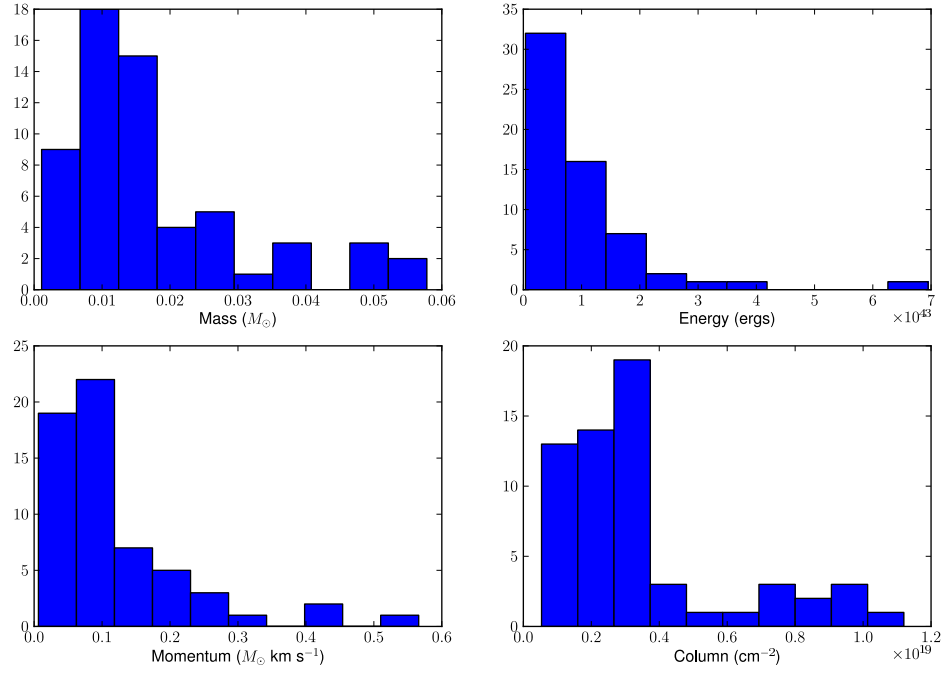


FIG. 10.— Histograms of outflow properties.

TABLE 1  
CO 3-2 OUTFLOWS

Outflow Number	Latitude	Longitude	Velocity center (km s <sup>-1</sup> )	Velocity min	max	1.1mm source	Mass (M <sub>☉</sub> )	Momentum (M <sub>☉</sub> km s <sup>-1</sup> )	Energy (ergs)	Association
1b	136.4437	1.2622	-35.485	-47.6	-40.3	G136.456+01.268	0.024	0.186	1.52×10 <sup>43</sup>	2MASS 02470195+
1r	136.4674	1.2705	-35.612	-31.9	-23.4	G136.456+01.268	0.0267	0.171	1.24×10 <sup>43</sup>	2MASS 02470195+
2r	136.4743	1.2042	-36.145	-31.7	-23.0	G136.512+01.194	0.00812	0.0547	4.17×10 <sup>42</sup>	none
3	136.475	1.2548	-35.551	-31.8	-26.8	G136.474+01.268	0.0162	0.115	8.9×10 <sup>42</sup>	2MASS 02470551+
2b	136.4899	1.1904	-35.799	-48.0	-39.7	G136.512+01.194	0.0196	0.0989	5.27×10 <sup>42</sup>	none
4b	136.5086	1.2622	-35.202	-44.1	-40.1	G136.500+01.258	0.00856	0.0549	3.62×10 <sup>42</sup>	none
4r	136.5109	1.2751	-35.409	-32.4	-28.6	G136.500+01.258	0.00765	0.0297	1.19×10 <sup>42</sup>	none
5r	136.5113	1.2454	-35.036	-31.4	-28.8	G136.500+01.258	0.0155	0.0916	5.69×10 <sup>42</sup>	K1223?
5b	136.5236	1.2524	-34.85	-45.0	-39.2	G136.500+01.258	0.00631	0.0293	1.38×10 <sup>42</sup>	K1223?
6b	136.532	1.228	-34.778	-44.8	-40.0	G136.536+01.232	0.00623	0.0432	3.06×10 <sup>42</sup>	2MASS 02472805+
6r	136.5321	1.2328	-34.739	-30.6	-24.0	G136.536+01.232	0.00786	0.0559	4.2×10 <sup>42</sup>	2MASS 02472805+
7b	136.5449	1.2327	-34.687	-47.5	-39.9	G136.536+01.232	0.0157	0.126	1.06×10 <sup>43</sup>	K1388
7r	136.5498	1.2386	-34.784	-29.9	-22.7	G136.536+01.232	0.0133	0.0994	7.89×10 <sup>42</sup>	K1388
8b	136.5795	1.2745	-34.9	-41.5	-39.3	none	0.0302	0.183	1.15×10 <sup>43</sup>	K1688
8r	136.581	1.2601	-35.297	-30.0	-23.9	none	0.0191	0.102	6.04×10 <sup>42</sup>	K1688
9b	136.67	1.2123	-34.638	-44.5	-38.5	G136.671+01.210	0.0116	0.0505	2.38×10 <sup>42</sup>	K2038
9r	136.6766	1.2059	-34.663	-31.6	-26.7	G136.671+01.210	0.0473	0.29	1.85×10 <sup>43</sup>	K2038
10b	136.7172	0.7859	-43.267	-52.6	-47.5	G136.719+00.782	0.0355	0.237	1.61×10 <sup>43</sup>	K1100
10r	136.7271	0.7797	-43.44	-38.1	-33.1	G136.719+00.782	0.0306	0.123	5.32×10 <sup>42</sup>	K1100
11r	136.8173	1.0799	-34.29	-31.4	-20.4	G136.828+01.064	0.0158	0.102	7.96×10 <sup>42</sup>	K2500
11b	136.8196	1.0795	-34.29	-40.7	-37.0	G136.828+01.064	0.0203	0.12	7.73×10 <sup>42</sup>	K2500
12b	136.8414	1.1512	-42.56	-53.3	-46.2	G136.849+01.150	0.00951	0.091	8.78×10 <sup>42</sup>	K2861
13	136.8461	0.8426	-34.557	-31.0	-23.5	G136.842+00.838	0.0138	0.0851	5.67×10 <sup>42</sup>	none
12r	136.8479	1.1517	-42.533	-34.6	-30.1	G136.849+01.150	0.0088	0.0606	4.44×10 <sup>42</sup>	K2861
14	136.8591	1.176	-42.573	-54.5	-47.1	G136.846+01.168	0.0377	0.265	2.09×10 <sup>43</sup>	K3022?
15	136.9458	1.0835	-41.102	-55.0	-45.0	G136.948+01.092	0.0218	0.139	9.71×10 <sup>42</sup>	none
16b	137.3937	0.5954	-39.966	-45.6	-42.6	G137.394+00.610	0.0445	0.395	3.84×10 <sup>43</sup>	K5648,5697
16r	137.3971	0.6112	-40.008	-37.0	-33.3	G137.394+00.610	0.0553	0.388	2.93×10 <sup>43</sup>	K5648,5697
17	137.4083	0.6763	-39.851	-57.9	-44.1	G137.409+00.674	0.0205	0.112	6.45×10 <sup>42</sup>	K6202
18b	137.4813	0.639	-35.318	-42.5	-39.4	G137.479+00.640	0.00313	0.0126	5.17×10 <sup>41</sup>	K6733
18r	137.4935	0.6324	-35.278	-30.9	-28.2	G137.479+00.640	0.00561	0.0247	1.13×10 <sup>42</sup>	K6733
19	137.5008	0.6172	-35.76	-44.7	-40.9	G137.479+00.640	0.0137	0.109	1×10 <sup>43</sup>	none
20r	137.5356	1.279	-37.875	-33.0	-22.5	G137.538+01.278	0.00741	0.0403	2.21×10 <sup>42</sup>	K10566
20b	137.5382	1.2786	-37.86	-49.2	-41.8	G137.538+01.278	0.000791	0.00453	2.63×10 <sup>41</sup>	K10566
21b	137.6139	1.3533	-39.245	-52.0	-43.7	G137.617+01.350	0.00202	0.0128	8.19×10 <sup>41</sup>	K11604
21r	137.6193	1.3603	-39.245	-35.2	-30.0	G137.617+01.350	0.0144	0.0528	2.17×10 <sup>42</sup>	K11604
22	137.6215	1.5045	-38.307	-46.0	-40.3	G137.632+01.508	0.025	0.143	9.06×10 <sup>42</sup>	K12110?
23r	137.6389	1.5251	-38.3	-42.5	-40.5	G137.665+01.526	0.0253	0.212	1.88×10 <sup>43</sup>	K12334
23b	137.6449	1.5194	-38.3	-36.5	-32.0	G137.665+01.526	0.00844	0.0596	4.41×10 <sup>42</sup>	K12334
24r	137.7094	1.4824	-38.808	-33.8	-25.4	G137.707+01.490	0.0341	0.216	1.45×10 <sup>43</sup>	K12648
24b	137.7146	1.4809	-38.653	-50.0	-42.7	G137.707+01.490	0.014	0.148	1.59×10 <sup>43</sup>	K12648
25b	138.1403	1.6841	-38.589	-49.5	-43.2	G138.144+01.684	0.044	0.519	6.4×10 <sup>43</sup>	K16614
25r	138.142	1.6884	-38.561	-34.3	-27.5	G138.144+01.684	0.0159	0.185	2.24×10 <sup>43</sup>	K16614
26b	138.2913	1.5538	-38.229	-52.0	-47.4	G138.295+01.556	0.00729	0.0452	2.82×10 <sup>42</sup>	K17020
26r	138.2966	1.5564	-38.156	-30.0	-20.0	G138.295+01.556	0.0146	0.14	1.38×10 <sup>43</sup>	K17020
27	138.3017	1.5689	-38.122	-30.0	-22.0	G138.295+01.556	0.0108	0.0719	4.89×10 <sup>42</sup>	confused
28	138.3042	1.5437	-38.204	-46.1	-43.3	G138.295+01.556	0.00983	0.0777	6.26×10 <sup>42</sup>	confused
29	138.3053	1.5537	-38.169	-51.6	-45.3	G138.295+01.556	0.0138	0.11	8.89×10 <sup>42</sup>	confused
30	138.3115	1.5443	-38.234	-33.0	-29.2	G138.295+01.556	0.0158	0.103	7.11×10 <sup>42</sup>	confused
31	138.3184	1.5566	-38.066	-49.1	-44.4	G138.295+01.556	0.016	0.117	9.48×10 <sup>42</sup>	confused
32	138.3213	1.5658	-37.863	-31.7	-27.0	G138.295+01.556	0.00435	0.0177	7.49×10 <sup>41</sup>	confused
33b	138.3622	1.5048	-39.101	-49.5	-44.0	none	0.00296	0.0175	1.07×10 <sup>42</sup>	K17125
33r	138.3642	1.4959	-38.758	-34.7	-25.8	none	0.00849	0.0738	6.66×10 <sup>42</sup>	K17125
34r	138.4779	1.6137	-37.216	-33.1	-29.1	none	0.00827	0.0754	7.19×10 <sup>42</sup>	confused
34b	138.478	1.6139	-37.216	-43.6	-40.6	none	0.0151	0.115	9.46×10 <sup>42</sup>	confused
35r	138.4998	1.6496	-37.816	-31.3	-24.1	G138.502+01.646	0.00867	0.059	4.21×10 <sup>42</sup>	confused
35b	138.5021	1.6458	-37.795	-49.5	-43.6	G138.502+01.646	0.00627	0.0471	3.59×10 <sup>42</sup>	confused
36b	138.5034	1.6654	-37.336	-50.4	-42.3	G138.502+01.646	0.00499	0.0218	9.58×10 <sup>41</sup>	confused
36r	138.5061	1.6576	-37.365	-32.6	-26.7	G138.502+01.646	0.0509	1.31	3.39×10 <sup>44</sup>	confused
37r	138.5208	1.6618	-37.331	-33.5	-31.4	none	0.0102	0.0278	8.33×10 <sup>41</sup>	K17644?
37b	138.526	1.6651	-37.334	-47.0	-43.6	none	0.00478	0.0124	3.47×10 <sup>41</sup>	K17644?
38b	138.6143	1.5611	-59.59	-71.1	-61.7	none	0.00655	0.0182	5.19×10 <sup>41</sup>	K17719
38r	138.6158	1.563	-59.59	-57.6	-54.5	none	0.003	0.0152	7.77×10 <sup>41</sup>	K17719

<sup>a</sup>Outflow properties and source associations.

TABLE 2  
TOTALS OF OUTFLOW PROPERTIES

BGPS source	1.1mm mass $M_{\odot}$	Intensity (K km s <sup>-1</sup> )	Outflow Column (cm <sup>-2</sup> )	Outflow Mass ( $M_{\odot}$ )	Momentum ( $M_{\odot}$ km s <sup>-1</sup> )	Energy (ergs)
G136.456+01.268	19.81	1.657	$5.45 \times 10^{18}$	0.0507	0.357	$2.76 \times 10^{43}$
G136.474+01.268	15.06	0.832	$2.74 \times 10^{18}$	0.0162	0.115	$8.9 \times 10^{42}$
G136.500+01.258	38.16	2.166	$7.11 \times 10^{18}$	0.03802	0.2055	$1.188 \times 10^{43}$
G136.512+01.194	85.65	1.512	$4.97 \times 10^{18}$	0.02772	0.1536	$9.44 \times 10^{42}$
G136.536+01.232	88.86	2.744	$9.03 \times 10^{18}$	0.04309	0.3245	$2.575 \times 10^{43}$
G136.671+01.210	71.31	2.667	$8.78 \times 10^{18}$	0.0589	0.3405	$2.088 \times 10^{43}$
G136.719+00.782	81.3	4.28	$1.407 \times 10^{19}$	0.0661	0.36	$2.142 \times 10^{43}$
G136.828+01.064	224.1	2.51	$8.25 \times 10^{18}$	0.0361	0.222	$1.569 \times 10^{43}$
G136.842+00.838	21.84	0.813	$2.67 \times 10^{18}$	0.0138	0.0851	$5.67 \times 10^{42}$
G136.846+01.168	67.96	2.05	$6.74 \times 10^{18}$	0.0377	0.265	$2.09 \times 10^{43}$
G136.849+01.150	133.2	1.34	$4.4 \times 10^{18}$	0.01831	0.1516	$1.322 \times 10^{43}$
G136.948+01.092	202.8	1.45	$4.76 \times 10^{18}$	0.0218	0.139	$9.71 \times 10^{42}$
G137.394+00.610	26.68	5.38	$1.768 \times 10^{19}$	0.0998	0.783	$6.77 \times 10^{43}$
G137.409+00.674	41.22	1.06	$3.48 \times 10^{18}$	0.0205	0.112	$6.45 \times 10^{42}$
G137.479+00.640	107.5	1.839	$6.047 \times 10^{18}$	0.02244	0.1463	$1.1647 \times 10^{43}$
G137.538+01.278	87.68	0.545	$1.793 \times 10^{18}$	0.008201	0.04483	$2.473 \times 10^{42}$
G137.617+01.350	128.2	1.358	$4.466 \times 10^{18}$	0.01642	0.0656	$2.989 \times 10^{42}$
G137.632+01.508	48.13	2.29	$7.52 \times 10^{18}$	0.025	0.143	$9.06 \times 10^{42}$
G137.665+01.526	65.13	3.16	$1.04 \times 10^{19}$	0.03374	0.2716	$2.321 \times 10^{43}$
G137.707+01.490	71.2	1.763	$5.78 \times 10^{18}$	0.0481	0.364	$3.04 \times 10^{43}$
G138.144+01.684	201.7	3.63	$1.193 \times 10^{19}$	0.0599	0.704	$8.64 \times 10^{43}$
G138.295+01.556	824.4	6.957	$2.289 \times 10^{19}$	0.09247	0.6825	$5.3999 \times 10^{43}$
G138.502+01.646	361.7	4.899	$1.613 \times 10^{19}$	0.07083	1.4379	$3.47758 \times 10^{44}$

<sup>a</sup>Totals of outflow mass, momentum, and energy associated with BGPS sources.



TABLE 3  
FLUX/MASS TOTALS IN SUB-REGIONS

Region name	Longitude	Latitude	1.1 mm flux (Jy)	CO flux (K km s <sup>-1</sup> )	1.1 mm mass ( $M_{\odot}$ )	CO mass ( $M_{\odot}$ )
S201	138.4976	1.6443538	3.2	12	170	970
AFGL4029	138.2375	1.6204152	6.6	24	340	1900
LWCas	137.65329	1.4164703	4.9	31	260	2400
W5NW	136.59104	1.2462782	1.5	41	77	3300
W5W	136.89115	1.1063707	6.1	34	320	2700
W5S	137.43528	0.63446173	0.39	2	20	210
W5SW	136.77721	0.81833915	0.32	6	17	480
Inactive2	137.13316	1.3124234	0.26	23	13	1800
Inactive1	137.85337	1.7364642	0.62	9	32	770
Inactive3	137.94131	0.79845766	0.0	5	0	410
empty	138.00234	1.3953913	0.29	2	15	180
W5All	137.36323	1.1324553	34.0	330	1800	26000